Nuclear Instruments and Methods in Physics Research B 269 (2011) 57–68

Contents lists available at ScienceDirect

Nuclear Instruments and Methods in Physics Research B

journal homepage: www.elsevier.com/locate/nimb

A GUPIX-based approach to interpreting the PIXE-plus-XRF spectra from the Mars Exploration Rovers: I. Homogeneous standards ☆

J.L. Campbell [a,*], J.A. Maxwell [b], S.M. Andrushenko [a], S.M. Taylor [c], B.N. Jones [d], W. Brown-Bury [a]

[a] Guelph-Waterloo Physics Institute, University of Guelph, Guelph, Ontario, Canada N1G 2W1
[b] 3A 47 Surrey St. East, Guelph, Ontario, Canada N1H 3P6
[c] Dept. of Atmospheric and Oceanic Sciences, McGill University, Montréal, Québec, Canada H3A 2K6
[d] Surrey Ion Beam Centre, University of Surrey, Guildford GU2 7XH, UK

ARTICLE INFO

Article history:
Received 22 July 2010
Received in revised form 5 October 2010
Available online 13 October 2010

Keywords:
Particle-induced X-ray emission analysis
X-ray fluorescence analysis
Alpha-particle X-ray spectrometer
Compton and Rayleigh scattering
Calibration

ABSTRACT

A new fitting code has been developed on the basis of GUPIX for application to alpha-particle X-ray spectrometers, which employ simultaneously two excitation mechanisms – XRF and PIXE – for elemental analysis of a single sample, and which are principal analytical instruments on the Mars Exploration Rovers. We present some of the basic aspects of our approaches to spectrum fitting, and we use a subset of the original calibration spectra from the MER mission to test our approach to standardization. This test is limited to results from homogeneous standards such as pure elements, oxides and chlorides, and simple minerals that comprise a single phase. The important, additional issues of multiple mineral phases that arise when geochemical reference materials are used as standards are dealt with in the subsequent paper. It is shown that an accurate standardization can be achieved with only minimal resort to empirical corrections. Attention is paid to fitting of the Compton scatter feature and to the extraction of the Compton–Rayleigh scatter ratio, because the latter quantity is the basis of our method for determining "invisible" light element (water, ice and carbonate) content of Martian samples.

1. Introduction

The Mars Exploration Rovers (MER) Spirit and Opportunity have been reporting elemental analyses of Martian basaltic rocks and soils, sediments, and various highly sulfated samples since they landed in 2004. The instrument responsible is the alpha-particle X-ray spectrometer (APXS), which deploys two well-known beam interaction techniques simultaneously for analysis of the sample under study; these are PIXE (particle-induced X-ray emission) and XRF (X-ray fluorescence). The APXS is accompanied on each rover by a panoramic camera, a Mossbaüer spectrometer and a miniature thermal emission spectrometer. This group of instruments has been responsible for major advances in the understanding of the Martian surface, especially as regards the prior existence of water on that planet [1]. An APXS will be part of the instrument suite on the Mars Science Laboratory (MSL) mission, which is intended to explore areas rich in phyllosilicates, sulfates and hematites [2]. Further development of the APXS for future planetary missions is very likely. Its established importance and future potential justify an in-depth effort to develop as rigorous as possible an approach to fitting the spectra and extracting element concentrations in geological samples. We report in detail on our progress in this effort in this paper and the subsequent one [3].

The MER APXS design of Rieder et al. [4] is presented schematically in Fig. 1. Six disc sources of the radionuclide ^{244}Cm, each having activity approximately 20 MBq, are arranged in a circle around a zirconium aperture behind which resides a silicon drift detector (SDD). The 5.806 MeV alpha particles, reduced to energy approximately 5.15 MeV by titanium cover foils and by the Martian atmosphere, provide the PIXE analysis. The L X-rays of the daughter plutonium atom provide the XRF analysis. The alpha particles are ideally suited for the ionization of the important light, major elements sodium, magnesium, aluminum and silicon, but the strong dependence of the ionization cross-sections upon the atomic number Z causes a rapid decrease in sensitivity (signal per unit concentration) with increasing Z. Conversely, the 14–20 keV L X-rays are optimum for the photo-electric excitation of the heavier elements such as iron and zinc, but the XRF sensitivity decreases strongly with decreasing Z. The combination of PIXE and XRF is thus highly complementary, providing a sensitivity that varies much more slowly than that of either method alone across the

☆ Based in part on invited talks delivered at the 19th International Conference on Ion Beam Analysis, Cambridge, UK, 2009 and the 12th International Conference on PIXE, Surrey, UK, 2010.

* Corresponding author. Tel.: +1 519 824 4120x52325; fax: +1 519 836 9967.
E-mail addresses: icampbel@uoguelph.ca, jlc@physics.uoguelph.ca (J.L. Campbell).

0168-583X/$ - see front matter © 2010 Elsevier B.V. All rights reserved.
doi:10.1016/j.nimb.2010.10.004

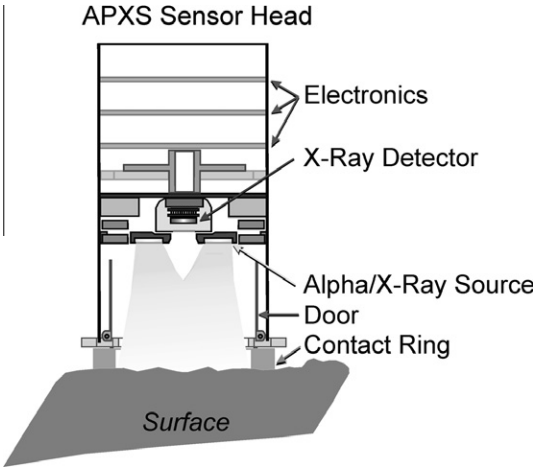

Fig. 1. Schematic of the alpha particle X-ray spectrometer.

range of atomic numbers ($11 < Z < 39$) that is of geochemical and mineralogical interest. The sensitivity is a minimum at $Z \sim 21$, where both excitation mechanisms are contributing approximately equally.

The upper panel of Fig. 2 shows the spectrum of a phyllosilicate reference material taken with a laboratory APXS which is one of a triplet of almost identical MER instruments, two of which were deployed on Mars. The regions of energy where the characteristic X-rays arise mainly from PIXE and mainly from XRF are marked. Towards higher X-ray energies we observe the contribution of plutonium Lα X-rays which are scattered elastically (Rayleigh) and inelastically (Compton) from the sample into the detector. The MER APXS units were designed [4] to have an upper energy limit of ~16 keV, and so the plutonium Lβ and Lγ scatter peaks are not included in their spectra.

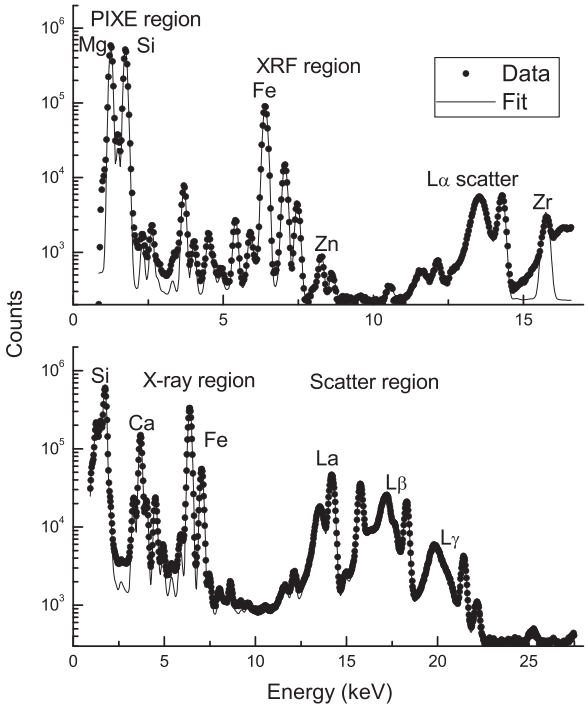

Fig. 2. Upper panel: representative spectrum (phyllosilicate reference material UB-N) from the MER APXS laboratory instrument; Lower panel: Spectrum of basalt reference material BR from MSL APXS.

The original calibration of the MER APXS instruments by Gellert et al. [5] was accomplished through use of an extensive primary suite of "standards" which included a sub-group of geochemical reference materials (GRMs) and a sub-group of simple chemical compounds. Several mineral, meteorite, and "blind" samples were used in secondary work. Their spectra were fitted using a dedicated least-squares peak-fitting code based on Minuit [6], which provided the area of the principal X-ray peak of each detectable element. Matrix corrections were then performed to account for X-ray attenuation effects within each GRM. For a given element, this matrix correction was taken to be a linear combination of an XRF matrix correction and a zero correction, with a weighting factor between these. While, at first sight, an XRF matrix correction might appear inappropriate for the light elements whose X-rays are excited by PIXE, the XRF approach is in fact a good approximation, as demonstrated by Rieder et al. [7]. For each element, an iterative optimization procedure was applied to determine the best values of the weighting parameter and of a "response" parameter, the latter being defined as the ratio between that element's X-ray counts and concentration in the absence of matrix effects. The value of the weighting parameter for each element was optimized by demanding linearity in the relationship between the certified and determined concentration values. A third parameter, the ratio between the attenuation coefficient μ in the standard for the X-ray of the element in question and the mean value of μ across the entire standard suite, was employed in this computation. Obviously, this approach to the matrix effects is somewhat empirical, especially as regards the weighting factor. Beyond the deletion of obvious outliers, there was no attempt in Ref. [5] to probe for any systematic differences among different types of standard, e.g. among different rock types within the subset of GRMs. The resulting calibration was applied to the results from Martian samples. The elemental concentrations for some 400 Martian samples, based on this approach, are stored on NASA's Planetary Data website [8].

Our work on the topic of APXS calibration commenced when the Principal Investigator for the MER APXS development suggested that we should develop a new approach to fitting APXS spectra, based upon the existing PIXE code GUPIX [9,10] as a starting point. This implies combination of a fundamental parameters approach with the use of standards, referred to hereafter as an FPS approach. There is clearly merit in developing a second and independent approach to complement the existing approach. Our approach is now well advanced, and we have reported a re-calibration of the MER laboratory instrument [11]. It has the additional major benefit of the ability to determine the content of "X-ray invisible elements" such as carbon, OH or H_2O by using the intensities of the Compton and Rayleigh scatter peaks in the spectra. This has enabled us [12] to estimate the hydration content of the light-toned, high-sulfur Paso Robles soils which were spun up from below the surface in the Columbia Hills area by the rover wheels.

Our FPS approach differs in several ways from that of Ref. [5]:

(i) Rather than determining a set of calibration parameters individually for each element, our objective in the present paper is to determine a single calibration factor (H) for the instrument as we have already done for PIXE [10];
(ii) Rather than effecting an empirical matrix correction after determination of the peak areas, we incorporate both the XRF and PIXE matrix effects rigorously from first principles within the spectrum fitting code. This is the approach used in GUPIX [9,10].
(iii) Rather than averaging a response parameter for a given element across all the pertinent standards in the two sub groups that comprise the primary suite of Ref. [5], we shall examine individually the results for each element in each standard. This will enable us to detect trends in the data that

may help us to refine the calibration and to ascertain in the special case of the GRMs the degree to which the calibration is influenced by their individual mineralogies.

(iv) Our earlier approach [11] to the calibration relied principally upon those GRMs in the suite of Ref. [5] which had been certified by national organizations. This reflects the fact that calibration with certified geochemical standards often is deemed preferable by the geochemical community to use of other standard materials or of fundamental parameters. However, in the work described in this and in the following paper, we refine and re-focus this approach. We continue to use Gellert's two main sub groups of primary standards defined in Ref. [5]. But, in this first paper, we generate a preliminary calibration of the instrument solely from the sub-group which comprises simple chemical element and compound standards; these materials can be considered homogeneous in the sense that they comprise a single chemical phase. We add to this sub-group four of the mineral materials that were used as secondary standards by Gellert et al. [5]; each of these is a single mineral phase and they provide a valuable addition to the set of homogeneous standards. This approach complies with the fundamental assumption of PIXE and XRF analysis that the distribution of atoms at the sub-micron level is uniform. In turn, this ensures that our standardization will reflect only the underlying atomic physics and the physical properties of the instrument. Exclusion, at this stage, of the GRMs, many of which contain multiple mineral phases, ensures that issues of matrix heterogeneity do not cloud our conclusions. The empirical approach of Ref. [5] does not enforce this separation; it averages its results across the entire group of GRMs and simple chemical standards.

Our ultimate objective is to ascertain the accuracy of the FPS approach for the analysis of unknown rock types. This will depend in part upon the accuracy of the physics database and the accuracy of our knowledge of the X-ray detector properties. We must anticipate that incomplete knowledge in either of these areas may necessitate the introduction of empirical corrections.

In the following paper [3], we then investigate the manner in which different classes of geochemical reference material obey or depart from this calibration. While our original work was based only upon the fully certified GRMs, we now add four geochemical reference materials which are not certified by national agencies, and a "blind" GRM. This enables us to extend the list of multiple mineral phase issues beyond those noted by us in Ref. [11], and, using X-ray diffraction analyses of the GRMs, to better understand these issues. In turn, this work provides an opportunity to refine the calibration such that different variants apply for different rock types.

2. The GUAPX methodology

2.1. Formalism

The GUPIX code, developed originally for proton beams [9,10], is widely used by the PIXE community and has been extensively tested. Alpha particle capability was added more recently [13], using both the ECPSSR and the reference ionization cross-sections of Paul and Bolik [14]; tests of this capability are much less numerous [15] but in the present work we find that the reference cross-sections are to be preferred. As a first step, we developed an analogous code GUXRF for X-ray fluorescence, augmenting the GUPIX database with the necessary photo-ionization cross-sections [16]. GUXRF has much in common with the widely used X-ray fluorescence code AXIL [17]. In a final step, GUPIX and GUXRF were merged to form GUAPX.

In either PIXE or XRF, the intensity or yield $Y(Z)$ of a particular characteristic X-ray line of an element Z having concentration C_Z in an infinitely thick sample can be written as

$$Y(Z) = N\Omega C_Z F_{AP}(Z) M(Z,\ \mathrm{geom})[t_Z \epsilon_Z] \quad (1)$$

Because the literature provides extensive discussion of the details of this equation in both PIXE and XRF [9,18], we will discuss it in a general, rather than a detailed, fashion. N is the number of incident ions or photons. Ω is the detection solid angle. The "atomic physics term" $F_{AP}(Z)$ combines the atomic mass of element Z, Avogadro's number N_{av}, the atomic fluorescence yield ω_Z, and the branching ratio b_Z for the particular diagram line of interest; this quantity is a function of properties of the element of interest only. Thus

$$F_{AP}(Z) = N_{av}\omega_Z b_Z / A_Z \quad (2)$$

The term M separates out the influence of the sample matrix on the incoming ion or photon and on the outgoing X-rays of the element of interest; it is dependent upon the entry angle of the excitation radiation and the exit angle of the characteristic radiation, hence the presence of the descriptor "geom". Here we are using the word "matrix" in its normal sense within the context of ion beam analysis. In the PIXE case, the matrix term involves energy-dependent ionization cross-sections, the matrix stopping power for the incoming helium ions and the matrix attenuation coefficient for the outgoing X-ray. In the XRF case, it involves photo-ionization cross-sections and the matrix attenuation coefficients for both incoming and outgoing X-rays. The matrix term is therefore dependent upon all the elements present and their concentrations; this prevents the direct deduction of a given C_Z value from the corresponding measured $Y(Z)$ value in an unknown sample.

At this point, we must re-iterate that our FPS method and the method of Ref. [5] share an important, common assumption regarding the homogeneity of the material (standard or sample) being analyzed. The computation of the term M can only be fully accurate if the atoms of the sample are homogeneously distributed on the sub-micron scale of distance; this is often expressed as the requirement that the matrix must be homogeneous. In rocks, which may contain several different mineral phases, this requirement is violated. To invent an example, some alpha particles incident on a basalt sample may encounter feldspar grains, while others encounter pyroxene grains; given that the depth probed is only a few microns, it is clear that what is being sampled is not a uniform distribution of the atoms that comprise feldspar and pyroxene. This is why the present paper focuses only upon materials where there is near certainty that our definition of homogeneity prevails. This use of this term in the ion and photon beam analysis context should not be confused with its other use, which demands that the amount of sample actually analyzed should be sufficient to ensure that it is representative of the bulk material from which the particular sample has been is selected. But again, the very small ranges of the alpha particles indicate that this second issue can not be set aside.

Finally, the square bracket in Eq. (1) contains the X-ray transmission fraction t_Z through any absorbing materials such as the Martian CO_2 atmosphere, and the intrinsic efficiency ε_Z of the SDD.

In shifting from the beam excitation situation to the radionuclide excitation situation, the number of ions is replaced by the source activity and the measurement duration T. We can merge the source activity and the effective detector solid angle into a single instrumental constant H, such that

$$Y(Z) = HC_Z T F_{AP}(Z) M(Z, \mathrm{geom})[t_Z \epsilon_Z] \quad (3)$$

Although ^{244}Cm decay produces two distinct alpha particle energies, these are so close in value that the single weighted mean energy may be used. The plutonium daughter emits, through the

internal conversion process, an X-ray series that comprises some twenty L diagram lines. If f_L is the fraction of decays that produces an L X-ray, then the total X-ray yield can be written as

$$Y(Z) = Y_{PIXE}(Z) + \sum Y_{XRF}(Z) \quad (4)$$

where

$$Y_{PIXE}(Z) = H\, C_Z\, T\, F_{AP}(Z) M_{PIXE}(Z,\ \mathrm{geom})[t_Z \epsilon_Z] \quad (5)$$

and

$$Y_{XRF}(Z) = f_L\, H\, C_Z\, T\, F_{AP}(Z) M_{XRF}(Z, \mathrm{geom})[t_Z \epsilon_Z] \quad (6)$$

The term $F_{AP}(Z)$ is determined from the GUPIX database. A noteworthy change which we made to the database was the upward adjustment of the K-shell fluorescence yield of the elements sodium, magnesium, aluminum and silicon by 7% when they are bound within oxides or silicates. This was based upon the experimental observations of Campbell et al. [19], who attributed the effect to the influence of chemical bonding upon the outer electrons. The instrumental constant H must be determined experimentally with known standards or reference materials (see Section 2.4). It is obviously implicit in our approach that there needs to be an understanding of all factors which determine the detector efficiency as a function of X-ray energy. The most recent experimental determination of f_L for ^{244}Cm [20] agrees within 1.5% with the value that is deduced from the ^{244}Cm decay scheme [21] using recently published nuclear and atomic data [22,23]. The relative intensities of twenty-five plutonium L X-ray lines were also determined from published experimental and theoretical data [21–24]. Lines which contributed less than 0.1% to the total intensity were then omitted, the total neglected contribution being 0.3%. The remaining intensities, re-normalized to a total of 100%, are given in Table 1.

In conventional PIXE and XRF work, the geometry is well-defined, in that the exciting beam enters the sample at a unique angle to the surface, and the excited (characteristic) beam exits also at a unique angle. This idealized situation clearly does not exist in the APXS, where (see Fig. 1) each of these angles has a range of possible values. This issue has been dealt with in our earlier development of a Monte Carlo code MELISSA [25] which employs the GUPIX and GUXRF X-ray production sub-routines to predict the X-ray intensities for each element that would be expected from a given sample in a defined APXS geometry. It contains an optimization scheme which enables the user to deduce a pair of "effective angles" of entry and exit which would result in the same total X-ray intensities. These effective angles were used in the present work.

Table 1
Energies and relative intensities (sum = 1.00) of the fifteen most intense plutonium L X-ray lines emitted in the decay of ^{244}Cm.

Line	Energy (keV)	Relative intensity
Ll	12.124	0.0247
Lα2	14.084	0.0394
Lα1	14.279	0.3457
Lη	16.334	0.0103
Lβ1	18.294	0.3584
Lβ4	17.557	0.0022
Lβ3	18.541	0.0018
Lβ6	16.498	0.0064
Lβ15	17.208	0.0084
Lβ2	17.255	0.0768
Lβ7	17.705	0.0016
Lβ5	17.946	0.0171
Lγ5	20.708	0.0029
Lγ1	21.418	0.0863
Lγ6	22.151	0.0178

2.2. Spectrum fitting details

We are concerned here with fitting the calibration spectra from the MER APXS project. The upper limit of these spectra [5] was set between the plutonium Lα and Lβ groups, as shown in the upper panel of Fig. 2. No such limit has been imposed in the MSL APXS, a spectrum from which is in the lower panel. Further work required to fit the additional plutonium L lines in the MSL context will be mentioned below.

The fitting procedure is the slightly modified Marquard non-linear least-squares method taken directly from GUPIX. Two variables A_1 and A_2 are introduced to define the linear relationship between channel number C and X-ray energy E (in keV):

$$C = A_1 + A_2 E \quad (7)$$

Two further variables A_3 and A_4 similarly define the relationship between the Gaussian peak width (standard deviation in channel units) σ and X-ray energy:

$$\sigma^2 = A_3 + A_4 E \quad (8)$$

The approach thus assumes a linear response and takes advantage of the high accuracy with which characteristic X-ray energies are known [26]. This is important as regards achieving accurate separation of overlapping peaks.

There is one further variable for each element which contributes X-rays to the model spectrum; this is the height of its most intense X-ray line (usually $K\alpha_1$ or $L\alpha_1$). For a given element, all the other diagram and satellite lines have their intensities coupled to the principal line's intensity through the literature relative intensities which are stored in the database; these relative intensities are modified by the absorber/efficiency term and by the matrix term in Eqs. (4)–(6). While the peak shape is assumed to be Gaussian, the choice does exist in GUAPX to adopt Voigtian lineshapes should the counting statistics justify this. Silicon escape peaks and pile-up peaks are treated precisely as in GUPIX [9,10].

In the middle region of the spectrum, the background continuum arises mainly from the long low-energy tails of the plutonium L X-ray peaks. It is obvious from Fig. 2 that the plutonium Lα scatter doublet is sitting on such a feature, generated by the Lβ and Lγ groups. These tails arise partly from Compton scattering interactions with core electrons, where the energy loss incurred in K-shell ionization is several keV. A second tailing contribution arises from incomplete charge collection (ICC) within the detector. At very low X-ray energies, the rising background with decreasing energy reflects the summation of ICC contributions from the more intense peaks. Secondary electron bremsstrahlung from the helium ions is the third contributor, confined mainly below a kinematic upper limit of 2.5 keV. The summed background from these three main contributors (there is also a very small "natural" background) is complex, even more so than in conventional PIXE or XRF analysis. For PIXE, we decided at an early stage in the development of GUPIX to abandon attempts to model such backgrounds, in favor of an advanced digital filter technique [27], whose earlier versions were based on existing approaches in X-ray fluorescence analysis. This approach removes not only the background from the three cited components but also the shelf features on the low-energy side of the X-ray peaks. Use of the digital filter method eliminates the need for further variables to be introduced into the fitting process. It has the consequence that the chi-squared test of goodness-of-fit is carried out between the filtered measured spectrum and the filtered model spectrum.

At present, we fit the Compton peaks of the plutonium Ll and Lα X-rays with an approximation that is similar, but not identical, to that introduced by Van Gysel et al. [28]. It consists of a Gaussian with a single exponential tail on the low-energy side. Four

Compton parameters are therefore needed in the first instance – peak height, ratio of peak width relative to the resolution width, tail height and tail slope. However, given the very low intensity of the Ll peak, it is assigned the same parameters as Lα, with the exception of its height. There are thus five parameters for the Ll,α group, four for the Lβ group, and four for the Lγ group. More sophisticated approaches under development are discussed in Section 4 below.

2.3. Physical Characteristics of the SDD

The manufacturer (Ketek GmbH) of the SDDs used in the MER project provided values for the silicon wafer thickness (0.28 mm), the window thickness (5 μm), the aluminum contact thickness (0.1 μm) and the gap length (1.8 mm) between the window and the crystal; this gap is filled with nitrogen at 1 bar pressure. A zirconium collimator is incorporated, with aperture diameter 2.5 mm. Neglecting issues of imperfect charge collection, these parameters define the detector efficiency in Eqs. (4)–(6), using the simple efficiency model that is incorporated in GUPIX. The impact of incomplete charge collection is discussed in Section 3.4 below.

The window of the SDD presents us with a problem. The material is dura-beryllium, which is a 5 μm beryllium foil coated with a proprietary protective layer of a low-*Z* material. We do not know the additional X-ray attenuation due to the coating. We must therefore anticipate that our calculated efficiency at very low X-ray energies will be over-estimated.

2.4. Standardization for elemental analysis

With standards or reference materials, the C_Z values are known a priori. In this special case, the GUAPX code computes the matrix terms once at the outset, and then iterates the fit to a minimum chi-squared value. This approach is referred to as the fixed-matrix (FM) approach. The instrumental constant H then is deduced simply by comparing the code's output concentrations with the known values. This approach tests the database and the detector description. Any imperfections in these may give rise to the need for Z-dependent corrections within Eqs. (4)–(6). In Section 3.4, we present details of the determination of the H-value by this approach, using a set of homogeneous standards.

2.5. Elemental analysis of unknown samples

In the case of unknown samples analyzed in the same geometry as the standards, we can have GUAPX use the H-value from Section 2.4 within the iterated-matrix (IM) approach which we first developed for the GUPIX code [10]. In the first iteration to optimize the goodness-of-fit, the C_Z values are not known and so the sample is treated as infinitely thin, such that the matrix has no influence. Out of this first fit come peak areas, i.e. X-ray yields, from which a first estimate of the full C_Z set is obtained through Eqs. (4)–(6). With these concentrations, the matrix terms for the X-rays of each element can be computed in a second iteration; the fit is optimized, and an improved set of C_Z values is obtained. This sequence, which involves iterating to a best fit within each successive matrix iteration, continues until the reduced chi-squared of the fit reaches a minimum and the concentrations are stable. Then a concluding linear least squares fit provides the final result.

At first sight, this iterated-matrix approach appears to be applicable only in the case where the X-rays of every element present are visible in the spectrum. In analyses of Martian geological materials, the X-rays of oxygen, which constitutes about 50 wt.% of most samples and GRMs, are "invisible". This forces us to adopt the widely-used approach of conventional XRF known as the "closure rule" [29], as was also done by Gellert et al. [5]. The element concentrations from GUAPX in iterative-matrix mode are converted to oxide concentrations via assumed stoichiometry, and the user is then given a choice as to whether the oxide total is accepted or is normalized to 100 wt.%. In the particular situation of a fixed sample-detector geometry, the proximity of the un-normalized total to 100 wt.% is a useful criterion of quality. This use of the closure rule renders the absolute H-value redundant, but any Z-dependent corrections determined as in Section 2.4 are certainly not redundant.

2.6. Use of the Compton/Rayleigh ratio to detect "X-ray invisible" components (water, CO_2, etc.)

We have developed a Monte Carlo method [30] which predicts the intensity ratio (C/R) between the Compton and Rayleigh scatter peaks. This calculation requires the system's geometric details and the measured element concentrations as input. It uses tabulated Compton and Rayleigh cross-sections [31], and takes full account of multiple scattering and matrix effects. This enables us to derive a quantity K which we define as the ratio between the measured (fitted) and predicted C/R values for any given standard or sample. A sequence of small improvements by Lee [32] to our original code has refined the accuracy of the K-values that we determined for Gellert's geochemical reference materials [5]. The K-values of unknown samples may be compared to the GRM calibration in order to infer the presence or absence of an "invisible" component such as water.

3. Characterization of the laboratory MER APXS

3.1. Introductory remarks

During their calibration of the MER laboratory APXS, Gellert et al. [5] recorded spectra from a diverse set of "standards", which were mostly in powder form with the exception of a few solid materials. The powders were sieved to exclude grains over 75 μm in diameter, and then spread in a sample holder with care to achieve as smooth a surface as possible. The overall standard suite included: (i) various pure elements and simple chemical compounds, listed in Table 2; (ii) several mineral samples; (iii) twenty-five GRMs, of which twenty-three had certified concentrations and two had provisional concentrations from national government laboratories; (iv) four meteorite samples; (v) three "in-house" GRMs from the Max-Plank-Institüt fur Chemie in Mainz, Germany, (vi) five "blind" samples provided by NASA's Jet Propulsion Laboratory. The actual standardization of Ref. [5] was accomplished with a primary subset of these, namely the groups (i), (iii) and (v), together with a single mineral sample and a single meteorite sample.

3.2. Peak widths and the Fano factor

In fitting the MER APXS spectra of the simple chemical standards of group (i), we allowed the parameters $A_1 \ldots A_4$ to vary in each case. The peak widths are plotted versus energy in Fig. 3. The peak width in energy units (eV) is given by

$$\sigma^2 = \sigma_n^2 + F\,\varepsilon\,E \tag{9}$$

where the first term on the right is the electronic noise contribution and the second is the hole-electron statistical term including the Fano factor F and the energy per hole-electron pair ε. The slope of this plot gives the $F\varepsilon$ product as 0.466. With ε set at the accepted value of 3.8 eV, this gives $F = 0.120 \pm 0.002$, which is in reasonable

Table 2
Ratio R of measured and nominal concentrations in simple element, compound and mineral standards. The physical form[a] was solid (S) or powder (P). The measurements were performed under either 0 or 10 mbar pressure of carbon dioxide. Brackets indicate anomalies.

Z	Measurement	Form, pressure	R
11	NaCl	P, 0	0.886
	NaCl	P, 10	0.862
	Na_2CO_3	P, 10	0.896
	Na_2CO_3	P, 0	0.922
	Na_2SO_3	P, 10	0.822
	NaBr	P,10	(0.67)
	Albite	P,10	0.909
12	MgO	P, 0	1.002
	MgO	P, 10	(0.717)
	$MgSO_4$	P, 0	0.926
	$MgSO_4$	P, 10	0.950
13	Al_2O_3	P,10	(0.886)
	Al_2O_3	P, 0	(0.904)
	Al_2O_3	S, 0	1.008
	Al	S, 0	1.029
	Albite	P, 10	1.016
	Anorthite	P, 10	0.963
	Orthoclase	P, 10	1.026
14	SiO_2	P, 0	1.004
	SiO_2	P, 10	0.979
	SiO	S, 0	1.024
	SiO	P, 0	1.001
	Albite	P, 10	0.977
	Orthoclase	P, 10	0.993
	Anorthite	P, 10	1.014
15	Apatite	P, 0	0.871
	Apatite	P, 10	0.874
	$Ca_3(PO_4)_2$	P, 10	0.897
16	$MgSO_4$	P, 0	0.933
	$MgSO_4$	P, 10	0.973
	Na_2SO_3	P, 0	0.913
17	NaCl	P, 0	0.984
	NaCl	P, 10	0.956
19	K_2CO_3	P, 10	(0.825)
	KBr	P, 10	(0.9)
	$KBrO_3$	P, 0	(0.89)
	KCr_2O_7	P, 10	0.976
	Orthoclase	P, 10	.991
20	$CaCO_3$	P, 0	(1.053)
	$CaCO_3$	P, 10	1.023
	Apatite	P, 0	1.006
	Apatite	P, 10	1.010
	$Ca_3(PO_4)_2$	P, 10	(1.066)
	Anorthite	P,10	1.014
22	TiO_2	P, 0	1.004
24	Cr_2O_3	P, 10	1.034
	KCr_2O_7	P, 10	0.958
25	MnO	P, 10	1.003
26	Fe	S, 0	1.005
	Fe_2O_3	P, 0	1.008
	Fe_2O_3	P, 10	1.005
28	Ni	S, 0	1.001
	NiO	P, 10	0.986
29	CuO	P, 10	0.975
30	ZnO	P,10	1.053
35	NaBr	P, 10	0.992
	KBr	P,10	0.981
	$KBrO_3$	P,0	0.992

[a] Solid samples were approx. 1 mm closer than powder samples so R was corrected down by 1.074 (mean factor between solid and powder results where both forms were run) to allow for different solid angle.

agreement with the value of 0.115 reported by Leutenegger et al. [33] for a Ketek detector.

The reason behind this determination of the $F\varepsilon$ product was to permit us to reduce the number of variables in our eventual fits to spectra of standards and of geochemical reference materials. In a first set of these GRM fits, both A_2 and A_4 were allowed to vary. This enabled us to determine the mean value of A_2 and thence to deduce via Eq. (9) an A_4 value (0.442) which could then be held fixed throughout a subsequent, final set of fits to the GRM spectra. A_2 was permitted to vary in order to cope with small fluctuations in the energy calibration arising from ambient temperature changes, etc.

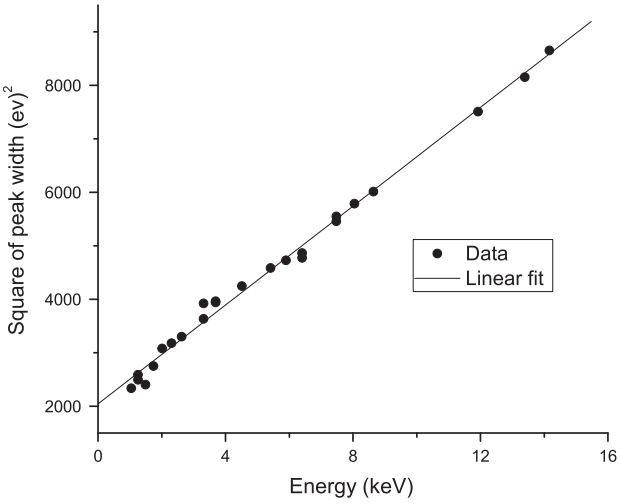

Fig. 3. Relationship between peak width and X-ray energy in the MER APXS laboratory instrument.

3.3. Shape of the iron K X-ray lines

The GUPIX code permits use of a variety of functional forms to describe the low-energy tailing features of the Gaussian lineshape. Because the iron K X-rays are often very intense in the GRM spectra, there is a possibility of inaccurate fitting of the weak manganese Kα line which is superimposed on the iron tailing feature. For the MER APXS, fits were done to iron metal spectra to establish the parameters of an exponential tail and a short step, which together provided a good description of the tail. These parameters then served as a fixed part of the iron lineshape when fitting the GRM spectra.

3.4. Determination of the H-value and the overall calibration

In our first work on re-calibration [11], we deliberately restricted ourselves to groups (i) and (iii) of the primary standard suite used by Gellert et al. [5]. As indicated in Section 1, our philosophy here has undergone a shift. In this paper we shall focus only on group (i) and a small subset of group (ii), i.e. on materials where we can be confident that each standard is comprised of a single chemical or mineral phase. This ensures homogeneity as defined in Section 2.1 above, which in turn should ensure that computed matrix terms are accurate. Relative to Ref. [11], we have deleted the standards of rubidium nitrate and strontium nitrate, which we now know to have been diluted with other materials; and we have added sodium bromide, potassium bromide, potassium bromate, and potassium chlorate, which had previously been omitted.

Among the GRMs, the elements of highest concentration excited by PIXE and XRF respectively are silicon and iron. Within groups (i) and (ii), there are more data for silicon and iron than for other elements. There is therefore merit in using the data from one of these elements (we chose silicon) to determine the H-value, and then testing whether agreement results when this H-value is used for the other element. To accomplish this testing, we shall examine, for each element, the ratio R between the concentration determined by GUAPX and the true concentration.

In our earlier work [11] we derived the system *H*-value from four spectra recorded from SiO and SiO_2 samples in group (i). In the present work, we augment these silicon data by including spectra of three simple feldspar (framework silicate) minerals from group (ii), which both we and Gellert et al. [5] had previously excluded. One of these spectra is attributed to an albite sample. Albite is the end-member of the plagioclase feldspar group, with chemical formula $NaAlSi_3O_8$. This spectrum shows no detectable potassium or calcium, indicating that the sample is indeed pure albite, and enabling us to describe the fixed matrix accurately as $NaAlSi_3O_8$. The next mineral sample is described as orthoclase; pure orthoclase is the other end-member $KAlSi_3O_8$. However, this spectrum shows a sodium peak equivalent to 1.0 wt.% concentration, which tells us that there is a very small substitution of potassium by sodium. We therefore subtracted 1 wt.% from the formulaic potassium concentration to determine a value for the "true" potassium concentration, and repeated the FM fit to obtain final concentrations. In the third mineral sample, anorthite (nominally $CaAl_2Si_2O_8$), we find small contributions of both sodium (0.52 wt.%) and iron (0.64 wt.%). The Mineralogy Database [34] provides an empirical formula for orthoclase containing 0.41 wt.% sodium, viz. $Na_{0.05}Ca_{0.95}Al_{1.95}Si_{2.05}O_8$. Iron in feldspars is predominantly in the 3 + valence state and substitutes for aluminum in the crystal structure [35]. We therefore added 0.64 wt.% iron to the matrix and reduced the aluminum content by this amount, prior to performing the final FM solution.

These additional feldspar materials have two significant merits. First, they increase the number of silicon data points to seven (see Table 2). We used these data to establish an *H*-value such that the mean *R*-value for silicon is 1.00. Second, the consistency of the silicon data points engenders confidence in the accompanying six new data points provided by the three feldspars for sodium, aluminum, potassium and calcium. For calcium we now have seven data points in all, of which five are in very close agreement, with a mean *R*-value of 1.013. The seventh point, from calcium phosphate, differs by about 6%. We assume this to reflect a sample placement error and we use the 0.94 factor to re-normalize the phosphorus point from this standard. The resulting *R*-value for phosphorus agrees well with the phosphorus results from hydroxy-apatite, thereby providing some justification for the approach taken to the calcium phosphate result.

The *R*-values for all the other elements of all the standards in groups (i) and (ii), obtained with this *H*-value, are given in Table 2. Of the fifty-eight data points, seven are low outliers relative to the well-established overall trend. When a sample surface is not perfectly smooth (as is the case with these powder standards), the emitted X-ray intensity can be depressed, as shown in quantitative studies [36,37] for both modes of excitation. This might explain the anomalously low results for sodium and potassium in NaBr and KBr, where the X-rays of these elements are very strongly absorbed by the bromine partner. The Al_2O_3 case might be due to failure to remove all adsorbed water from this hygroscopic material.

With these outliers ignored, the average values of *R* for each element are then plotted against atomic number in Fig. 4, where the fitted curve is empirical. The silicon *R*-value is 1.00 by definition, the aluminum point agrees with unity within its uncertainty, and the mean of all data points in the region $22 \leqslant Z \leqslant 35$ is 1.00. Apparently, our approach gives the desired *R*-value of unity over much of the region, with only five elements exhibiting significant exceptions to this constancy. Errors in this assertion are at the level of 1–2%. There is a steep fall-off with decreasing *Z* for the three elements phosphorus, sulfur and chlorine, with the curve *R*(*Z*) then recovering to unity when silicon is reached. It is useful to note in each of these three cases that the second element of the compound used (calcium, magnesium and sodium respectively) follows the overall *R*(*Z*) trend in its own region, which we see as supporting

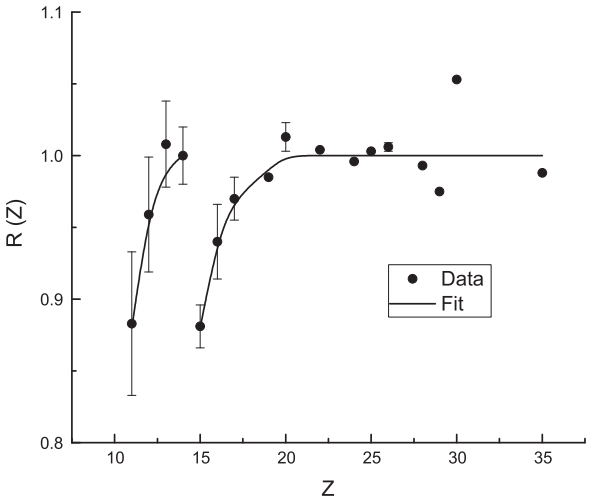

Fig. 4. Mean values of *R* for each element in the simple chemical and mineral standards.

the validity of the phosphorus, sulfur and chlorine data points. This observation strongly suggests that the detector has a layer of incomplete charge collection (ICC). A detailed discussion of the effect of such an ICC layer in silicon drift detectors for very low values of X-ray energy was recently given by Eggert et al. [38].

The second departure from unity in Fig. 4 occurs below aluminum. It is very likely that much of this effect is caused by our inability (discussed in Section 2.3) to include the dura-coating of the beryllium window in our detector model. Part of the effect must also arise from the ICC layer. The large spread in the sodium results is a further cause for concern; it may arise from surface roughness, which has the greatest effect at the lowest energies.

An extensive detector characterization exercise, such as that of Plagnard et al. [39], was not possible when the spectra that we are using here were generated by Gellert et al. [5]. Such an exercise would have provided an understanding of both the dura-beryllium window and the putative ICC layer, and would have enabled us to incorporate appropriate descriptions in the GUAPX file that determines the detector's intrinsic efficiency ε_Z for use in Eq. (6). Such an exercise is not now possible, because this detector type has been superseded. For the moment we are forced to resort to an empirical correction in our approach to standardization of the MER APXS for the elements concerned. We simply introduce a multiplicative factor *k*(*Z*) on the right-hand side of Eqs. (4)–(6). The results above show that this empirical correction factor is factor is unity except for the five elements sodium, magnesium, aluminum, phosphorus, sulfur and chlorine; for these cases it is defined as

$$k(Z) = R_{\mathrm{fit}}(Z) \tag{10}$$

This now provides us with a calibration that is summarized in Table 3, and which applicable to samples that are known to comprise a single chemical or mineral phase.

This resort to empirical corrections might appear to be at variance with our objective of developing a FPS approach. We counter

Table 3
MER APXS calibration parameters for homogeneous standards.

H	Z	k(Z)
0.0417	11	0.88
	12	0.96
	15	0.88
	16	0.94
	17	0.97

such a notion by pointing out that our approach has calibrated the instrument to accuracy well within 5% for most elements, and that the remaining five cases are understood qualitatively. For future instruments, a full detector characterization exercise should enable the production of *R*-values that are within a few percent of unity for all elements in the range $11 < Z < 38$. However, we must concede that the remarkable agreement between the silicon *R*-value and those of the elements in the region of iron may be fortuitous. The present results imply that there is very little error in our assumed PIXE and XRF cross-sections, but this is unlikely for the former of these. When the low-energy end of our R-curve is handled more rigorously, such that the sodium and magnesium values rise, the silicon value will also rise, and the agreement between silicon and the iron region will be worsened. If this is indeed what happens, then the most likely cause will be the accuracy of the PIXE cross-sections.

4. Detailed fitting study of the scatter region in the MER APXS spectra

To date, we have relied upon a modification of the empirical description suggested by Van Gysel et al. [27] for modeling the broad, asymmetric Compton scatter feature of the plutonium Lα X-rays in the MER APXS spectrum. Details were given in section 2.2 above. In the lower panel of Fig. 2 we show a fit to the spectrum of the basalt reference material BR taken with the advanced APXS model designed for the Mars Science Laboratory mission [40]. Four sets of Compton feature parameters (for each of Ll, Lα, Lβ and Lγ) are now required. The overall fit of the scatter region, which now includes the entire L X-ray series of plutonium, appears rather good. However, with the present description of the scatter feature, GUAPX over-estimates the concentrations of rubidium and strontium in GRMs, because of the overlaps between the rubidium Kα and the Compton peaks, and between the strontium Kα and the Rayleigh peaks. We are therefore working towards an improved model for the scatter region of the spectrum.

Fig. 5 shows the results of a Monte Carlo simulation of the Compton-scattered energy distributions from the individual subshells of silicon. The methodology was an extension of our previous work [29], limited to describing single scatter Compton events in the geometries of both the MER and MSL APXS instruments; detector resolution broadening has not been applied. The different high-energy cut-offs which are visible for each subshell reflect the fact that the scattered photon cannot have an energy that exceeds the difference between the incident energy of 14.28 keV and the relevant subshell binding energy. (Incidentally, these cut-offs are the reason for our deletion of Van Gysel's high-energy tail). The fractional contribution of each subshell to the total feature intensity for a given Z can be parameterized as a function of *Z* for all major and minor elements. For each subshell, the energy distribution can be fitted rather well by the sum of two Gaussians; the correlated height and width parameters of these two Gaussians can then be represented as parameterizations versus *Z*.

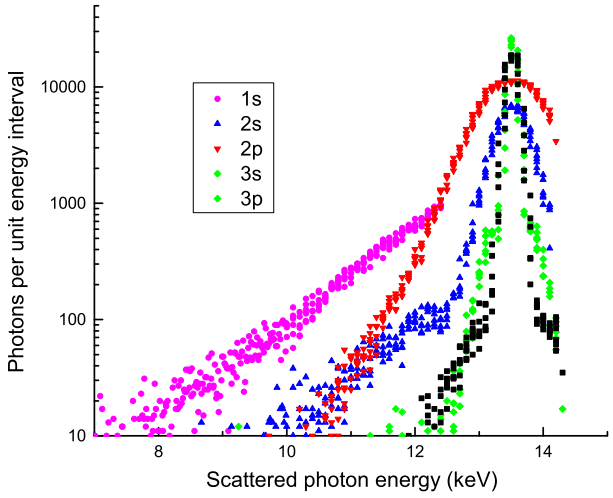

Fig. 5. Simulated energy distributions for 14.28 keV X-rays scattered from the subshells of silicon in the geometry of the MER APXS.

This exploratory work suggests an improved approach to representing and fitting the Compton feature in the measured spectra. Given the major and minor element concentrations determined by GUAPX for a given sample, the intrinsic Compton energy distribution can be determined using the above parameterizations, and it can then be convolved with the detector resolution function. Only one overall parameter (intensity) of this feature would have to be added to the variables of the fitting procedure. In fitting the extended spectra of the MSL APXS, the different energies of the Lα. Lβ and Lγ groups would be catered for through the energy-dependence of the parameterization. This approach has at least three disadvantages, however. First, it would not describe the small multiple scattering component. Second, it would be computationally intensive. Third, the database would have to be re-developed by simulation for each new APXS geometry.

We have therefore preferred, as the next step, to take the alternative approach of experimenting with empirical modifications of the Van Gysel description of the Compton feature. These have been tested using a small number of MER and MSL spectra from standards and from GRMs that contain zero or very little rubidium and strontium, whose K X-rays overlap the Compton and Rayleigh peaks respectively. Although the subshell distributions for a given element have distinct mean energies, the presence of many elements smears this effect, as does the detector resolution.

Fig. 6 compares our existing representation with two new ones as regards the goodness of fit to the scatter region of the MER APXS spectrum of the geochemical reference material UB-N. The comparison is approximate because a linear background is used, but is sufficient to demonstrate the main shortcomings of our existing Compton representation, which is simply a Gaussian with a single low-energy, Gaussian-convoluted, exponential tail. Such tails are widely used to describe the slight tailing seen on X-ray peaks due to incomplete charge collection in the detector. In the present case, we find that the GUAPX code needs to fit a much more intense tail (relative to the Gaussian height) in order to deal with the very broad Compton feature. The peak of this tail function is rather sharp and it results in visible misfits near the top and on the high-energy side of the Compton feature. The change to a double Gaussian with no tail rectifies this situation, but at the cost of introducing a slight misfit in the lower reaches of the tail. In the third variant, we introduce a high-energy cut-off to the double Gaussian feature: the position of the cut-off was determined in advance by examination of simulated Compton spectra with the detector resolution broadening included. The fit is changed slightly between the Compton and Rayleigh peaks and it is difficult to decide which variant is superior, although the physics embedded in our third variant is more correct. With the third function, the R/C ratios are about 1.5% larger than with the second function. Work is now in progress to embed these functions into the GUAPX code.

5. Mars-related aspects of GUAPX

5.1. The window transfer function

For the Mars Exploration Rover mission, Gellert et al. [5] devised a simple but elegant procedure to transfer the laboratory

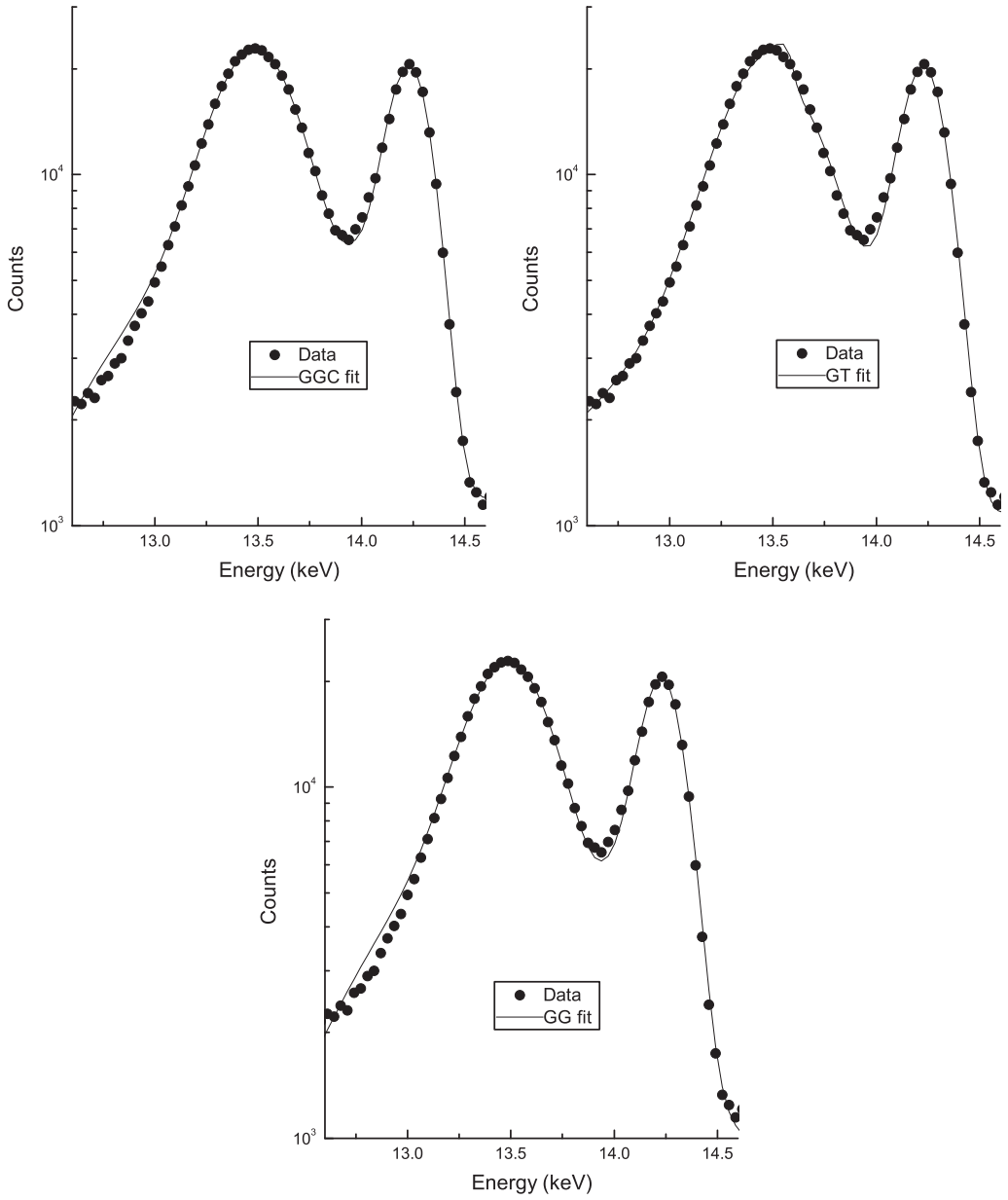

Fig. 6. Fits of empirical models to the Ll,α scatter region in the MER APXS spectrum of the reference material UB-N. GT = Gaussian + exponential tail; GG = double Gaussian; GGC – double Gaussian with high-energy cut-off.

instrument's calibration to the two flight models (FM1 and FM2). Spectra were recorded in the laboratory from each flight instrument using a small subset of the full standard suite. Then, for each element, the average ratio of peak counts per second between each flight model and the laboratory instrument was determined. While we prefer to calibrate in terms of concentration, their approach is easily adapted to our situation. Fig. 7 plots one of these two ratios, as determined by our GUAPX fits; it is similar, but not identical, to the plot of Ref. [5]. Our plot is interpreted as providing the ratio between the detection efficiencies in the two instruments, and its values are included in the detector description files for the two flight units. With this one change, the extensive calibration of the laboratory instrument is translated into the flight instrument calibration.

5.2. Effective angles of excitation and emission

In Section 2.1 we mentioned the Monte Carlo code MELISSA [25], which enables the user to deduce a pair of "effective angles" for entry of the exciting alpha particles and X-rays and for exit of the excited characteristic X-rays. These values are selected so that they result in the same total generated characteristic X-ray intensities as those computed by a rigorous Monte Carlo approach that takes full account of the ranges of these angles in the actual analytical geometry. The values determined for the two angles pertain, of course, to the geometry employed in the terrestrial calibration. The code has been updated and improved and we find that the resulting values (17° and 14°) are almost the same as previously (18° and 14°).

On Mars, however, the sample-detector distance varied from one sample to the next. Obviously, then, when Gellert et al. [5] used their terrestrial sensitivity factors to generate element and hence oxide concentrations, the latter usually did not sum to 100 wt.%. The oxide concentrations were therefore normalized to 100 wt.% sum. Gellert et al. refer to the normalization factor as the "geometric norm". Using our estimate (34.5 mm) of the terrestrial sample-detector distance and these geometric norm values,

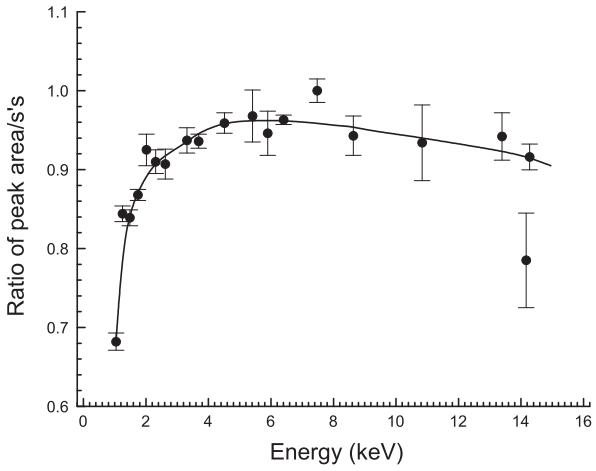

Fig. 7. Peak area ratio between flight model on Spirit rover and laboratory instrument.

we can compute the distribution of sample-detector distances for the Spirit rover, which are almost all in the range 30–60 mm; the Opportunity rover results are very similar. The question then arises as to whether or not the effective angle values have any significant dependence upon the sample-detector distance.

The MELISSA code was run at several sample distances up to 30 mm greater than the terrestrial calibration value. The results did not change sufficiently to justify making the effective angles functions of the distance. With unchanged angle values, the sodium K X-ray yield generated at 30 mm additional distance is 2.5% too large, the magnesium yield 0.6% too large, and all other elemental yields remain within 0.1% of their original values. These small changes reflect the strong attenuation of the X-rays of the lightest elements. The calibration approach of Gellert et al. [5] will be subject to the same small dependences upon sample-detector distance.

5.3. X-ray attenuation by the Martian atmosphere

The Martian atmosphere is 95% carbon dioxide, with the 6.1 mbar surface taken as the reference surface against which all elevations are measured. Although this pressure is small, it causes non-negligible attenuation of the X-rays emitted by the lightest elements in our analysis, so knowledge of the variations in pressure due to elevation of the rover and of the seasonal fluctuations are necessary to accurately analyze the X-rays from these elements. These are already difficult to characterize accurately due to the limitations of the instrument, so accurately describing the Martian atmosphere can help eliminate one source of significant error.

To characterize the atmosphere, a plot of data from the two Viking missions in the 1970's [41] was used. The data were fitted (and the fit discretized) by hand, and the two "baseline" pressures were determined. Since the elevations of the two Viking missions are known from Google Earth [42], the difference in average pressure between the two data sets was used to describe a linear pressure gradient with respect to height. The zero elevation surface is, in general, taken to be the 6.1 mbar surface; both the MER rovers lies below this surface. The elevation data for the MER rovers are also taken from Google Earth, this time by tracing the path of the rovers and using the embedded photographs to provide signposts (since otherwise it is unclear how long the rover took to travel between points). The elevations for Spirit vary by no more than about 85 metres, and the elevations of Opportunity vary very little, so these data are accurate enough for our measurements.

The seasonal variation is very clear in the Viking pressure data (the pressure can vary almost 1 mbar from the baseline pressure), and so for any given mission sol number, the orbital position, or index, of Mars must be known. This was done in a rather roundabout way using the Mars24 program [43]; there is no way to directly enter the mission sol number and get the orbital index Ls, so the mission sol number must first be converted to a Julian date, then entered into the program. A resolution of 20 sols was used, since Spirit and Opportunity landed 20 sols apart. The seasonal data from the Viking missions were normalized so that the baselines were equal and then averaged; this data set was used to calculate the pressure associated with a given spectrum.

To calculate the pressure for a given sample, then, the elevation and orbital positions are both found. The elevation gradient is used to calculate the elevation adjustment, and the seasonal pressure variation is linearly interpolated from the Viking data. These two corrections are added to the 6.1 mbar baseline pressure, to which all measurements are referred. The pressure is used to calculate the density of the atmosphere, which is then used with attenuation coefficient data from XCOM [44] to attenuate the low energy X-rays under consideration. The temperature is taken to be constant at 255 K; this is an average night-time temperature near the equator (where both Spirit and Opportunity are, and where the MSL rover is likely headed). The night-time temperatures range from around 230 K to around 280 K, and the density of the atmosphere can thus fluctuate up to almost 15% from the atmosphere at 255 K. There is no reliable way to know what the temperature was at the specific time a sample was taken, and since each spectrum was gathered over several hours, the temperature would probably vary significantly over each run.

There are various other assumptions and sources of error in this methodology: the data were fitted by hand, the pressure gradient is assumed to be linear, the other constituents of the atmosphere were not accounted for (nitrogen and argon comprise about 2.7 and 1.6 percent of the Martian atmosphere, respectively), and there is no accounting for the differences in latitude of the two rovers. By far the biggest source of uncertainty, though, is the uncertainty associated with the attenuation length. The rovers have no direct means to determine how far from each sample the instrument sits; currently, the distance can only be estimated from the discrepancy between the oxide total and unity, and that estimate is only valid for samples that contain no "X-ray invisible" components such as water.

These caveats suggest that the inclusion of the CO_2 attenuation correction may be somewhat academic at this time. Nonetheless we believe that it will be useful for future instrument versions where the variable sample-APXS distance is independently determined. We have made considerable progress in determining concentrations of X-ray invisible elements in the fixed geometry of the laboratory calibration exercise [45]. That work has shown that if the distance can be obtained independently, without reliance on the difference between the total oxide concentration and 100%, then the value of that difference becomes a valuable outcome of the analysis.

6. Conclusions and Prospects

From the viewpoint of ion beam analysis physics, the fundamental parameters approach described here, coupled with measurements on homogeneous "standards", appears to provide a satisfactory standardization of the instrument which is compatible with our understanding of it. The addition of several spectra of simple minerals to those of pure elements and chemical compounds was a valuable step, which consolidated the results for several of the lighter elements. Our hope that the MER APXS could be

calibrated with a single instrumental constant has almost, but not entirely, been borne out. Small corrections for five elements, admittedly empirical, but largely justifiable through a qualitative understanding of detector properties, were needed to complete the calibration. Synchrotron radiation characterization of future APXS detectors would enable the inclusion in our detector model of a quantitative description of the effects responsible. For the very lightest elements, there remain concerns with the database, in particular as regards the alpha particle ionization cross-sections and the effects of KL vacancy states on K-shell fluorescence yields. Careful basic physics work in these areas is needed if the remaining empirical aspects are to be minimized. Nevertheless, our approach appears to offer a useful complement to the existing spectrum analysis methodology of Gellert et al. [5].

From the viewpoint of a geochemist, the use of geochemical reference materials (GRM) certified by recognized "standards" providers is almost mandatory. Unfortunately, introduction of these materials brings the complication that they may be composed of more than one mineral phase, i.e. they may not satisfy the assumption of homogeneous atomic distribution. The standard suite used in the original MER APXS calibration exercise [5] included a large set of GRMs, which spanned various different rock types as regards mineralogy. Most of these types contain more than one mineral phase and thus do indeed have matrices that fail to satisfy the standard definition of homogeneity as used in ion beam analysis. The combination of this failure with the very small interrogation depths inherent in the PIXE process must render calibration via rock GRMs susceptible to error. While this issue was acknowledged in the original MER APXS calibration exercise of reference [5], no specific actions were taken to investigate it. The derived matrix corrections for each element were reached by an averaging process that spanned the entire standard suite, with the exception of outliers. These matrix corrections are thus based on a set of standards which includes both homogeneous and "multi-mineral" matrices. If variation in the modal mineralogy causes error, and if this error depends upon rock type, then these averaged matrix corrections would change if a different suite of standards was to be employed. While we have already raised this issue [11], the following paper [2] will investigate this important source of error in much more detail.

Accurate extraction of the useful C/R ratio from APXS spectra depends on having an accurate description of the asymmetric Compton scatter feature. Such a description would enable accurate measurement of small concentrations quantities of rubidium and strontium, which was not feasible hitherto. We have introduced a change to the empirical description of Van Gysel et al. [27], and shown that it gives significant improvement. This new approach is presently being installed in the GUAPX code.

Acknowledgements

This work was supported by the Natural Sciences and Engineering Research Council of Canada and the Ontario Centres of Excellence. B. Jones received partial support from the Canadian Space Agency and W. Brown-Bury received an NSERC post-graduate scholarship. We are very grateful to R. G. Rieder for introducing us to the challenge of APXS calibration and to R. Gellert for provision of the MER APXs data, continuing collaboration and excellent advice.

References

[1] J. Brückner, G. Dreibus, R. Gellert, S. Squyres, H. Wänke, A. Yen, J. Zipfel, Mars exploration rovers: chemical composition by the APXS, in: J. Bell (Ed.), Martian Surface, Cambridge University Press, 2008.
[2] J. L. Griffes, J. Grotzinger, J. Grant, A. R. Vasavada, M. Golombek, A. McEwen, Analysis of four potential Mars Science Laboratory landing sites using HiRISE, Abstracts of 40th Lunar and Planetary Science Conference (2009).
[3] J. L. Campbell, S. M. Taylor, G. M. Perrett, J. A. Maxwell, A GUPIX-based approach to interpreting the PIXE-plus-XRF spectra from the Mars exploration rovers: II geochemical reference materials, following paper.
[4] R. Rieder, R. Gellert, J. Brückner, G. Klingelhöfer, G. Dreibus, A. Yen, S. W. Squyres, The new Athena alpha particle X-ray spectrometer for the Mars exploration rovers, J. Geophys. Res., 108(E12) (2003), 8066–8079.
[5] R. Gellert, R. Reider, Brückner, B. C. Clark, G. Dreibus, G.Klingerhöfer, G. Lugmair, D. W. Ming, H. Wänke, A. Yen, J. Zipfel, S. Squyres, Alpha particle X-ray spectrometer (APXS): results from Gusev Crater and calibration report, J. Geophys. Res. 111, (2006) JE002555.
[6] F. James, M. Roos, MINUIT: Function minimization and error analysis, CERN D506, CERN, Geneva., 1989.
[7] R. Gellert, R.G. Rieder, G. Dreibus, G.W. Lugmair, R. Rieder, H. Wänke, J. Zipfel, J.L. Campbell, J. Maxwell, M. Omand. Notes on Alpha-Particle X-ray Spectrometer (APXS) Data Reduction. NASA Planetary Data System. http://pds-geosciences.wustl.edu/mer/mer2-m-apxs-2-edr-ops-v1/mer2ap_0xxx/calib/apxs_data_reduction.pdf.
[8] NASA Planetary Data System. http://pds-geosciences.wustl.edu/missions/mer/geo_mer_datasets.htm.
[9] J.A. Maxwell, J.L. Campbell, W.J. Teesdale, The Guelph PIXE software package, Nucl. Instrum. Methods Phys. Res., Sect. B 43 (1989) 218–230.
[10] J.A. Maxwell, W.J. Teesdale, J.L. Campbell, The Guelph PIXE software package II, Nucl. Instrum. Methods Phys. Res., Sect. B 95 (1995) 407–421.
[11] J.L. Campbell, M. Lee, B.N. Jones, S.M. Andrushenko, N.G. Holmes, J.A. Maxwell, S.M. Taylor, A fundamental parameters approach to calibration of the Mars exploration rover alpha particle X-ray spectrometer, J. Geophys. Res. 114 (2009) E04006.
[12] J.L. Campbell, R. Gellert, M. Lee, J.A. Maxwell, J.M. O'Meara, Quantitative in situ determination of hydration of bright high-sulfate Martian soils, J. Geophys. Res. 113 (2008) E06S11.
[13] T.L. Hopman, Z. Nejedly, J.A. Maxwell, J.L. Campbell, Extension of GUPIX to ^{2}H, ^{3}He and ^{4}He excitation, Nucl. Instrum. Methods Phys. Res., Sect. B 189 (2002) 138–142.
[14] H. Paul, O. Bolik, Fitted empirical reference cross-sections for K-shell ionization by alpha particles, Atomic Data Nucl. Data Tables 54 (1993) 75–131.
[15] S. Rohrs, T. Calligaro, F. Mathis, I. Orte.g.a-Feliu, J. Salomon, P. Walter, Exploring advantages of ^{4}He-PIXE analysis for layered objects of cultural heritage, Nucl. Instrum. Methods Phys. Res., Sect. B 249 (2006) 604–607.
[16] J.H. Scofield, UCRL report 51326 (1973).
[17] P. van Espen, H. Nullens, F. Adams, A computer analysis of X-ray fluorescence spectra, Nucl. Instrum. Meth. 142 (1977) 243–250.
[18] R. Van Grieken, A. Markowicz, Handbook of X-ray Spectrometry, Marcel Dekker, New York, 2002.
[19] J.L. Campbell, G.K. Czamanske, L. McDonald, W.J. Teesdale, Quantitiative analysis of major elements in silicate minerals and glasses by micro-PIXE, Nucl. Instrum. Methods Phys. Res., Sect. B 130 (1997) 608–616.
[20] P.N. Johnson, P.A. Burns, Absolute L X-ray intensities in the decays of ^{230}Th, ^{234}U, ^{238}Pu and ^{244}Cm, Nucl. Instrum. Methods Phys. Res., Sect. A 361 (1995) 229–239.
[21] R.B. Firestone, Table of Isotopes (8th edition), John Wiley Interscience: New York, 1996.
[22] I.M. Band, M.B. Trzhaskovskaya, C.W. Nestor Jr., P.O. Tikkanen, S. Raman, Dirac-Fock internal conversion coefficients, Atomic Data Nucl. Data Tables 81 (2002) 1–310.
[23] J.L. Campbell, Fluorescence yields and Coster-Kronig probabilities for the atomic L subshells, Atomic Data Nucl. Data Tables 85 (2003) 291–315.
[24] J.L. Campbell, J.-X. Wang, Interpolated Dirac-Fock values of L subshell X-ray emission rates including overlap and exchange effects, Atomic Data Nucl. Data Tables 43 (1989) 281–291.
[25] M. Omand, J.A. Maxwell, J.L. Campbell, Simulation of the relationship between elemental concentrations and X-ray yields in the Mars exploration rover's X-ray spectrometer, Nucl. Instrum. Methods Phys. Res., Sect. B 229 (2005) 123–136.
[26] R.D. Deslattes, E.G. Kessler Jr., P. Indelicato, L. de Billy, E. Lindroth, J. Anton, X-ray transition energies: new approach to a comprehensive evaluation, Revs. Mod. Phys. 75 (2003) 35–99.
[27] J.A. Maxwell, J.L. Campbell, Improvements to the top-hat filter approach for PIXE background removal, Nucl. Instrum. Methods Phys. Res., Sect. B 189 (2002) 143–147.
[28] M. Van Gysel, P. Lemberger, P. Van Espen, Description of Compton peaks in energy-dispersive X-ray fluorescence spectra, X-Ray Spectrom. 32 (2003) 139–147.
[29] H. Rollinson, Using Geochemical Data: Evaluation, Presentation, Interpretation, Pearson Education, UK, 1993.
[30] C.L. Mallett, J.M. O'Meara, J.A. Maxwell, J.L. Campbell, Calibration of the MER α-particle X-ray spectrometer for detection of "invisible" OH and H2O possibly present in Martian rocks and soils, X-Ray Spectrom. 35 (2006) 329–337.
[31] J.H. Hubbell et al., Atomic form factors, incoherent scattering functions, and photon scattering cross-sections, J. Phys. Chem. Ref. Data 4 (1975) 471–538.
[32] M. Lee, Private communication, 2009.
[33] P. Leutenegger, A. Longoni, C. Fiorini, L. Strüder, J. Kemmer, P. Lechner, S. Sciuti, R. Cesareo, Works of art investigation with silicon drift detectors, Nucl. Instrum. Methods Phys. Res., Sect. B 439 (2000) 458–470.

[34] Mineralogy Database. http://webmineral.com.
[35] W.A. Deer, R.A. Howie, J. Zussman, An Introduction to the Rock-Forming Minerals, Longman Scientific and Technical, UK, 1992.
[36] F. Claisse, C. Samson, Heterogeneity effects in X-ray analysis, Adv. X-Ray Anal. 5 (1962) 335–354.
[37] J.L. Campbell, R.D. Lamb, R.G. Leigh, B.G. Nickel, Effects of random surface roughness in PIXE analysis of thick targets, J.A. Cookson, Nucl. Instrum. Methods Phys. Res., Sect. B 12 (1985) 402.
[38] T. Eggert, O. Boslau, J. Kemmer, A. Pahlke, F. Wiest, The spectral response of X-ray detectors, Nucl. Instrum. Methods Phys. Res., Sect. B 568 (2006) 1–11.
[39] J. Plagnard, C. Bobin, M.-C. Lépy, Accurate efficiency calibration of a low-energy HPGe detector using a monochromatic X-ray source, X-Ray Spectrom. 36 (2007) 191–198.
[40] R. Gellert, Private communication, 2008.
[41] M.D. Smith, Spacecraft observations of the martial atmosphere, Annu. Rev. Earth Planet. Sci. 36 (2008) 191–219.
[42] Google Earth. http://earth.google.com/mars/.
[43] Mars24. http://www.giss.nasa.gov/tools/mars24/.
[44] M.J. Berger, J.H. Hubbell, S.M. Seltzer, J. Chang, J.S. Coursey, R. Sukumar and D.S. Zucker, XCOM: Photon Cross Sections Database, http://www.nist.gov/physlab/data/xcom/index.cfm.
[45] J.L. Campbell, S.M. Andrushenko, S.M. Taylor, J.A. Maxwell, A fundamental parameters approach to calibration of the Mars exploration rover alpha particle X-ray spectrometer: 2. Analysis of unknown samples, J. Geophys. Res. 115, E04009, doi:10.1029/2009JE003481.